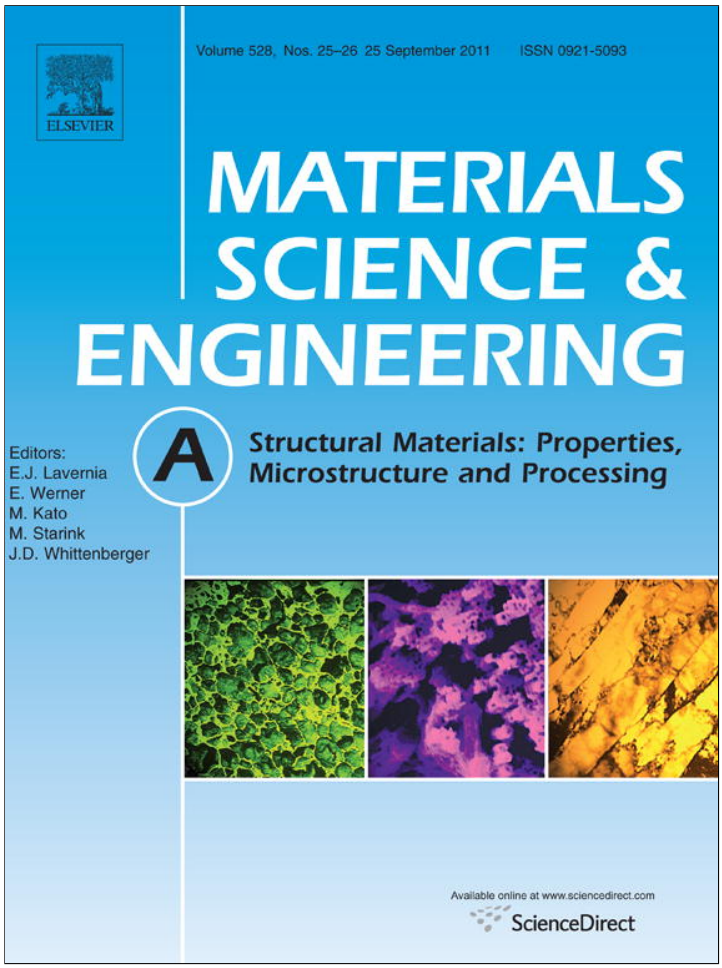

Materials Science and Engineering A 528 (2011) 7541–7551

Contents lists available at ScienceDirect

Materials Science and Engineering A

journal homepage: www.elsevier.com/locate/msea

# Radiation-induced segregation in austenitic stainless steel type 304: Effect of high fraction of twin boundaries

Parag Ahmedabadi[a,*], V. Kain[a], K. Arora[b], I. Samajdar[c], S.C. Sharma[d], S. Ravindra[c], P. Bhagwat[d]

[a] Materials Science Division, Bhabha Atomic Research Centre, Trombay, Mumbai 400085, India
[b] PEC University of Technology, Chandigarh, India
[c] Department of Metallurgical Engineering and Materials Science, Indian Institute of Technology Bombay, Mumbai, 400076 India
[d] Nuclear Physics Division, Bhabha Atomic Research Centre, Trombay, Mumbai 400085, India

ARTICLE INFO

*Article history:*
Received 25 February 2011
Received in revised form 18 May 2011
Accepted 22 June 2011
Available online 30 June 2011

*Keywords:*
EBSD
Austenite
Steel
Thermo-mechanical processing
Twinning

ABSTRACT

The effect of high fraction of twin boundaries on radiation-induced segregation (RIS) in type 304 stainless steel (SS) was investigated using 4.8 MeV proton beam at 300 °C. Type 304 SS samples were irradiated to 0.86 and 1.00 displacement per atom (dpa) and characterization of RIS was done using Electrochemical Potentiokinetic Reactivation (EPR) tests at different depth from the surface. Localized attack on different microstructural features, grain and twin boundaries and in-grain pit-like features, was further evaluated by atomic force microscopy. The results clearly indicated that attack was mostly confined to twin boundaries, implying that the twin boundaries acted as a preferred defect sink.



## 1. Introduction

The grain boundary engineering (GBE) approach involves increasing the fraction of special/twin boundaries in austenitic stainless alloys [1–3] through a suitable thermo-mechanical treatment. Various grain boundary phenomena viz. grain boundary diffusion [4], sliding [5], precipitation [6–8], corrosion [9,10], liquation [11], etc. depend on the grain boundary characteristics [12]. The GBE has been shown to improve the resistance to sensitization [13–17] and intergranular corrosion (IGC) [18–21]. Improved resistance to cracking [22] and an improvement in ductility [23] were also reported in grain boundary engineered material. Other studies have also reported [24–26] enhanced resistance to sensitization through randomization of grain boundaries. Special/twin boundaries are characterized as low Σ grain boundaries in the coincidence lattice sites (CSL) model [24]. The CSL boundaries are designated by a number Σ, which is the reciprocal of coincident sites [24]. The low energy (low Σ) boundaries are reported to have less susceptibility to solute/impurity segregation due to a more compact atomic structure [27,28].

Radiation-induced segregation (RIS) occurs due to diffusion of point defects (produced by irradiation) at the operating/testing temperatures and their segregation/depletion at grain boundaries by inverse Kirkendall and Interstitial Association Binding mechanisms [29–35]. RIS results [29] in segregation of silicon and phosphorus and depletion of chromium at grain boundaries. RIS is a part of a complex process that increases the susceptibility to irradiation assisted stress corrosion cracking (IASCC). The effect of grain boundary misorientation on RIS in austenitic stainless steel (SS) using proton irradiation had been reported earlier [36,37]. It was found [37] that the depletion of chromium was more for grain boundaries with higher Σ values while Σ3 boundaries had good resistance to chromium depletion due to RIS [36,37]. The effect of grain boundary misorientation on RIS in austenitic stainless steels was also studied using electron-irradiation [38] and numerical simulation [40]. It was found [38,39] that RIS had increased with increasing tilt-angle but suppressed at special boundaries like Σ3 and Σ9.

It may be noted that the effect of grain boundary nature on RIS was evaluated in the as-received austenitic stainless steels and not on thermo-mechanically processed or grain boundary engineered material. The fraction of twin boundaries in type 304 SS in solution-annealed condition would be much less than that in grain boundary engineered type 304 SS. In this investigation, effect of a high fraction of twin boundaries on RIS in grain boundary engineered type 304 SS material is evaluated using electrochemical potentiokinetic reactivation (EPR) test. In addition, effect of dose rate on the RIS is also evaluated. The EPR test is highly sensitive to the minimum level of chromium in the chromium depleted zones [41,42]. The EPR test had also been used to characterize the extent

* Corresponding author. Tel.: +91 22 25595402; fax: +91 22 25505151.
*E-mail address:* adit@barc.gov.in (P. Ahmedabadi).

0921-5093/$ – see front matter © 2011 Elsevier B.V. All rights reserved.
doi:10.1016/j.msea.2011.06.066

of RIS in austenitic stainless steels [43–49]. In this study, double loop EPR (DL-EPR) technique was used in combination with atomic force microscopic (AFM) examination to characterize the extent of RIS. It may be noted that analytical technique such as scanning transmission electron microscopy–energy dispersive spectroscopy (STEM–EDS) quantifies chromium depletion at an individual grain boundary whereas the EPR test quantifies chromium depletion on all the grain boundaries or at other microstructural features exposed to the EPR solution.

## 2. Material and experimental

### 2.1. Materials and processing

The material chosen for the present investigation was type 304 SS and obtained in the form of a 3 mm thick plate. The chemical composition (in wt%) of this alloy is C: 0.044, Cr: 19.97, Ni: 7.97, Si: 0.59, Mn: 1.85, P: 0.035 and S: 0.006. To achieve a high fraction of twin boundaries, the as-received (designated as AR) material was subjected to a pre-strain of 5% by uni-directional cold-rolling followed by strain-annealing at different temperatures for different time durations. Strain-annealing is an annealing treatment in which no new grain formation takes place, it only reduces the residual cold-work in the material. Five different strain-annealing treatments viz. 1027 °C for 0.5 and 1 h, at 927 °C for 24, 48, and 72 h were used. These combinations of thermo-mechanical treatments were chosen based upon a previous investigation [50] on type 304 SS. To study the effect of the alteration of grain boundary character distribution (GBCD) on sensitization, all the samples were given two potential sensitization heat-treatments viz. at 575 °C for 1 h (mild) and 675 °C for 1 h (severe). The DL-EPR tests on the heat-treated and the proton-irradiated specimen were carried out on the longitudinal surfaces. Specimens of dimension 12 mm × 12 mm were cut and ground using silicon carbide papers to a final finish by 2000 grit. Before proton-irradiation and electron backscattered diffraction (EBSD) measurements, samples were electropolished in 90% methanol, 10% perchloric acid solution at a temperature less than −30 °C to remove any surface deformation due to mechanical polishing.

### 2.2. Electron backscattered diffraction

The GBCD was obtained by EBSD in combination with orientation imaging microscopy (OIM) and measurements were done in FEI Quanta 200 HV and a Quanta 3d-FEG (field emission gun) scanning electron microscope (SEM). Both the SEM had TSL EBSD or OIM systems. Typically 3 mm × 3 mm areas were scanned in multiple scans, beam and video conditions were kept identical between the scans. In this investigation, grain boundaries with $\Sigma \leq 29$ were regarded as low $\Sigma$ boundaries and Brandon's criterion $\Delta\theta = 15^\circ \Sigma^{-0.5}$ was adopted [51] for the critical deviation in the grain boundary characterization.

### 2.3. Proton-irradiation

Of all combinations of thermo-mechanical treatments, the thermo-mechanical treatment that resulted in the lowest DL-EPR values (and the highest fraction of special/twin boundaries) for the mild and severe heat-treatments was chosen for proton-irradiation. Thermo-mechanically treated samples with the highest fraction of twin boundaries subjected to proton-irradiation are designated as ARTW. Irradiations were carried out using 4.8 MeV proton beam at 300 °C at a dose rate of $1.38 \times 10^{-6}$ or $5.342 \times 10^{-6}$ dpa/s (displacement per atom/second). Other experimental details are described in an earlier reported study [49]. The specimen with the lower dose rate was irradiated to 0.86 dpa and with the higher dose rate was irradiated to 1.00 dpa. The total area exposed to proton-irradiation was approximately 7 mm$^2$. The accumulated irradiation damage due to proton-irradiation, in terms of dpa, is calculated using NRT equation [52],

$$\text{dpa} = \frac{0.8}{2E_d}\left(\frac{dE}{dx}\right)_n \frac{\phi_t}{\rho}, \quad (1)$$

where $E_d$ is the displacement energy, $(dE/dx)_n$ is the linear energy transfer (LET) per ion/particle to target by nuclear processes, $\varphi_t$ is the fluence per unit area and $\rho$ is the atomic density. The damage profile obtained using SRIM for proton-irradiation was given a curve-fitting using Eq. (2),

$$y = a\left[c\left(\frac{1}{1+\alpha^2}\right) 1 + (1-c)\exp(-0.5\alpha^2)\right], \quad (2)$$

where $\alpha = (x - x_o)/b$ and $a$, $b$, $c$, $x_o$ are constants, $x$ is depth (in μm) and $y$ is the damage corresponding to given $x$.

### 2.4. Electrochemical characterization

The degree of sensitization (DOS) was evaluated using ASTM A 262 Practice A [53] and DL-EPR test [54]. The extent of RIS in proton-irradiated specimens was assessed using DL-EPR test. The details of electrochemical test used in this investigation are described in earlier reported study [49]. The optical microstructure obtained after ASTM A 262 Practice A test is classified [53] as 'step' (no regions on grain boundaries attacked), 'dual' (partial attack on grain boundaries) and 'ditch' (at least one grain completely surrounded by attacked grain boundaries) structure. The result of the DL-EPR test is reported as the DL-EPR value which is the ratio of the current in the backward loop to that in the forward loop, multiplied by 100. The maximum damage due to proton irradiation occurs at 74 μm below the surface for the proton energy of 4.8 MeV [55]. Therefore, starting from the as-irradiated surface, the DL-EPR test was repeated after removing the affected layer after each test, until the un-irradiated material was reached. After each DL-EPR test, the affected layer was removed by polishing using fine emery-paper followed with diamond paste of 0.5 μm. The thickness of specimens after each DL-EPR test was measured using a micrometer screw with a least count of 1 μm.

### 2.5. Atomic force microscopic examination

After the DL-EPR test, specimens were examined using NT-MDT Solver Pro scanning probe microscope in AFM mode in air using the semi-contact mode. The AFM scans were done on a 60 μm × 60 μm area and a number of scans were done for each DL-EPR test. The extent of attack during the DL-EPR test in the irradiated specimens was measured as depth of attack on various microstructural features like grain boundaries and twin boundaries and any other feature within the grains.

## 3. Results

### 3.1. Electron backscattered diffraction analysis

The fractions of special/twin boundaries in the AR and thermo-mechanically treated specimens are given in Table 1. The fraction of special boundaries ($\Sigma \leq 29$) and $\Sigma 3$ boundaries in the AR specimen was 0.54 and 0.28 respectively. For the specimen strain-annealed at 927 °C for 72 h after 5% pre-strain, the fraction of special boundaries had increased to 0.80; the fraction of $\Sigma 3$ was increased to 0.63 and the fraction of twins had increased to 0.54. The fraction of twins in the as-received material was 0.04. Fig. 1 shows an SEM micrograph for the specimen strain-annealed at 927 °C for 72 h, the presence of more than one twin in each grain is apparent. For annealing at

**Table 1**
Fraction of CSL boundaries and grain size for various annealing treatments after 5% cold-work.

| Annealing | $\Sigma \leq 29$ | $\Sigma 3$ | Random boundaries | Grain size (μm) |
|---|---|---|---|---|
| As-received | 0.54 | 0.33 | 0.46 | 18 |
| 1027 °C for 0.5 h | 0.59 | 0.49 | 0.41 | 33 |
| 1027 °C for 1 h | 0.50 | 0.34 | 0.50 | 44 |
| 927 °C for 24 h | 0.37 | 0.22 | 0.63 | 44 |
| 927 °C for 48 h | 0.45 | 0.34 | 0.55 | 42 |
| 927 °C for 72 h | 0.77 | 0.63 | 0.23 | 47 |

927 °C for different time durations, grain size increased from 18 μm (for the AR specimen) to 44 μm after 24 h of annealing and further increase in annealing time to 48 and 72 h did not result in any significant increase in grain size. The specimen strain-annealed at 927 °C for 72 h after 5% pre-strain is designated as ARTW.

It may be noted that both AR and ARTW samples were not completely strain free and this point was substantiated by the EBSD

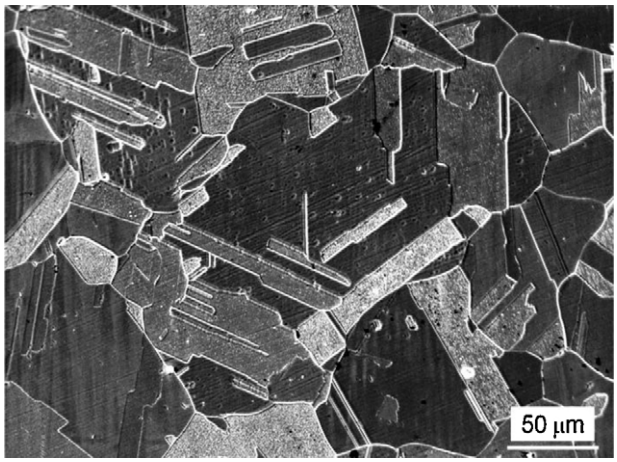


**Fig. 1.** Micrograph of the ARTW material after the DL-EPR test showing a high fraction of twin boundaries. Each grain has more than one twin.

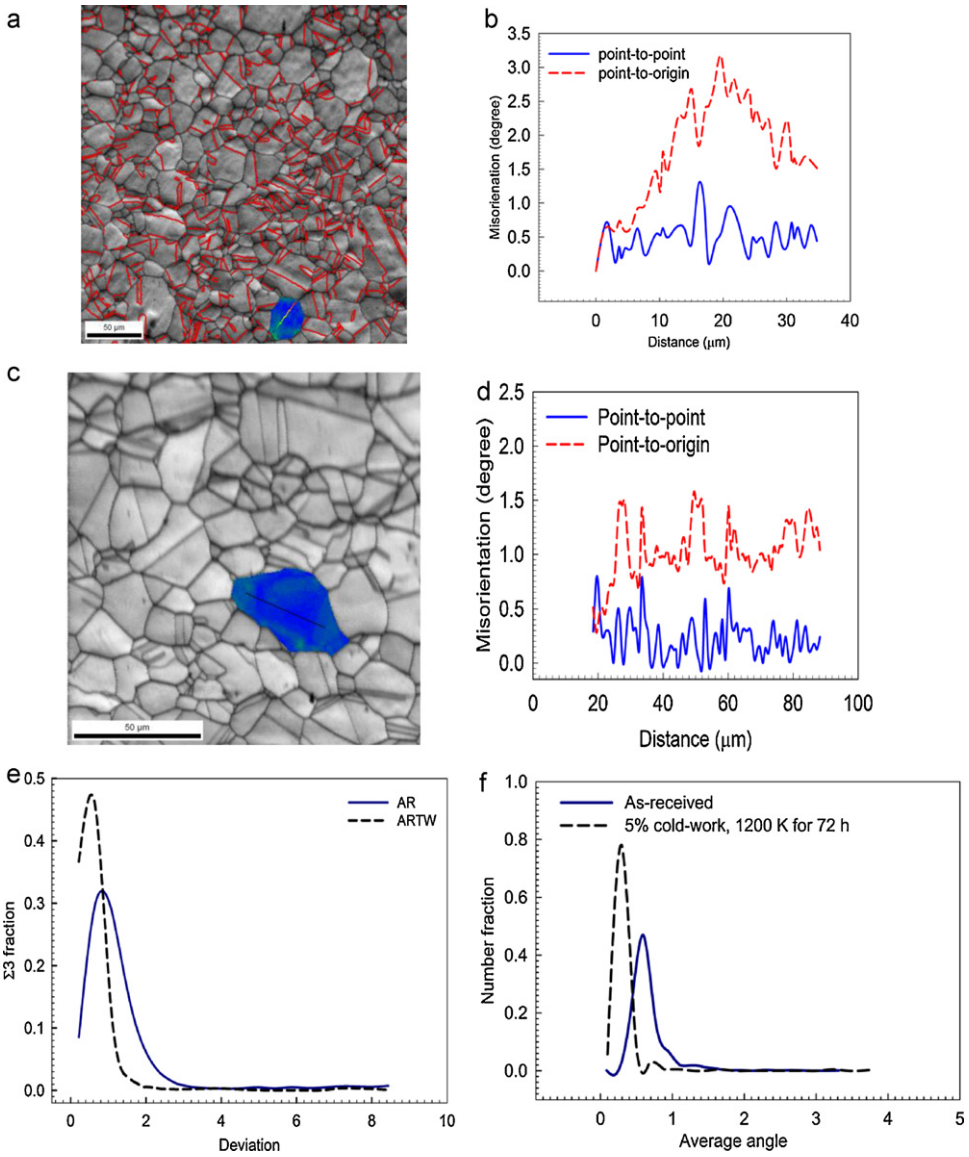


**Fig. 2.** Results of EBSD measurements showing (a) an EBSD image for the AR material and a profile-vector within a random grain (dark colour), (b) misorientation across a profile-vector in (a), point-to-point and point-to-origin measurements, large value of misorientation in the point-to-origin profile indicates residual strain within the material, (c) an EBSD image for the ARTW material and a profile-vector within a random grain (dark colour), (d) misorientation across a profile-vector in (c), point-to-point and point-to-origin measurements, the level of residual strain is less than that in the AR material, (e) comparison of the Σ3 deviation (according to Brandon's criterion) in the AR and ARTW material, the deviation had reduced in the ARTW. The average values for Σ3 deviation for the AR and ARTW material was 1.38 and 0.68, respectively, and (f) grain average misorientation (GAM) in the AR and ARTW material, with the average angle had reduced in the ARTW material.

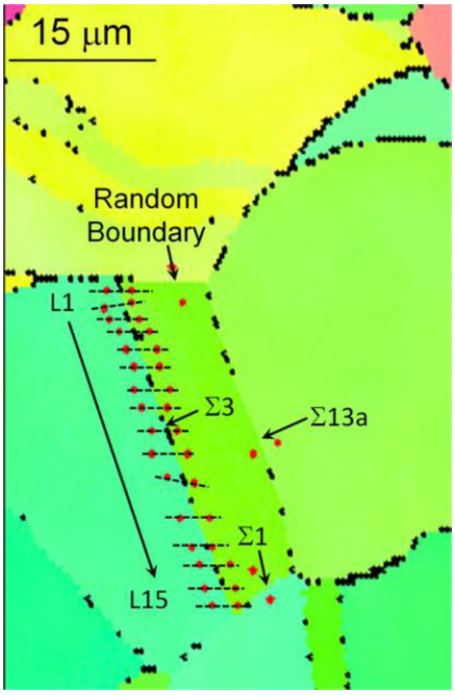


**Fig. 3.** An EBSD image for the ARTW material showing different types of boundaries viz. a twin boundary (Σ3), a Σ1 boundary, a Σ13a boundary, and a random boundary. The deviation from the 60°⟨1 1 1⟩ twin boundary condition at different locations (L1 to L15) was measured and reported in Table 2.

measurements as shown in Fig. 2. The line profiles on selected random grains show noticeable point-to-point (Fig. 2a and c) and point-to origin misorientation (Fig. 2b and d). The maximum values of these in fully annealed grains are 0.5° and 0.7°, respectively and can be taken as measurement uncertainty. The presence of misorientation, higher than the estimated measurement uncertainty, clearly shows the presence of residual strain. Residual strain was significantly lower, but not absent, in the ARTW sample. The hardness of the as-received specimen was 205 HV and that of the ARTW was 182 HV, which is close to typical hardness of completely solution-annealed type 304 SS of 180 HV. The annealing treatment at 927 °C for 27 h had reduced the statistical deviation from the ideal Σ3 in the ARTW sample. The maximum deviation of Σ3 boundaries due to thermo-mechanical processing had reduced from 1.38 (AR) to 0.68 (ARTW) as shown in Fig. 2e. The grain average misorientation (GAM) for the AR and ARTW specimens is shown in Fig. 2f. The higher GAM value for the as-received specimen also points to the presence of residual strain. The GAM value for the ARTW specimen was low (0.25) indicating lower residual strain.

Fig. 3 shows an EBSD image of the ARTW sample, showing a twin-boundary (Σ3), Σ1, Σ13a, and a random boundary. It may be noted that a twin boundary in fcc material like austenitic stainless steel is 60°⟨1 1 1⟩ boundary. The deviation from the ideal situation (i.e. 60°⟨1 1 1⟩ condition) for different locations (L1 to L15 in Fig. 3) is given in Table 2. The deviation from the ideal condition for a twin boundary is decreased for the locations away from a random boundary towards Σ1.

### 3.2. Sensitization behaviour

The DL-EPR values for the as-received, sensitization at 575 °C for 1 h, and 675 °C for 1 h were 0.07, 0.90 and 3.50, respectively. Table 3 gives the results of ASTM A 262, Practice A and DL-EPR tests for specimens with 5% pre-strain followed by different strain-annealing and heat-treatments. The DL-EPR values for sensitized specimens after various thermo-mechanical treatments are substantially lower than corresponding values for the AR material, as shown in Table 3. The highest resistance to sensitization was observed for annealing at 927 °C for 72 h after 5% pre-strain. The specimen annealed at 927 °C for 72 h showed a very low DL-EPR value as compared to the DL-EPR values after the other two annealing treatments at 927 °C. Fig. 4a shows the DL-EPR curve for the specimen annealed at 1027 °C for 0.5 h followed by sensitization at 575 °C for 1 h. As indicated by an arrow in Fig. 4a, an additional peak was noticed at a potential of −30 $mV_{SCE}$ (mV vs. saturated calomel electrode) during the forward scan. The specimen (5% pre-strain followed by 1027 °C for 0.5 h) was held at −30 $mV_{SCE}$ for 30 min in the EPR solution to examine the microstructural features responsible for the appearance of the peak at −30 $mV_{SCE}$. The microstructure obtained after the potentiostatic hold at −30 $mV_{SCE}$ is shown in Fig. 4b indicating preferential attack on strain-markings and twinned regions. This microstructure also reveals mirror-image markings indicating that such regions were probably twinned regions and not fully transformed into annealing twins. On the basis of the DL-EPR values and the fraction of special boundaries, ARTW (5% pre-strain and strain-annealing at 927 °C for 72 h) specimens were chosen to evaluate the effect of high fraction of twin boundaries on the RIS behaviour in type 304 SS.

**Table 2**
Deviation from the ideal condition (60°⟨1 1 1⟩) for a twin boundary at different locations shown in Fig. 3 in the ARTW specimen.

| Location | Sigma | Deviation |
|---|---|---|
| L1 | 3 | 3.1 |
| L2 | 3 | 3.7 |
| L3 | 3 | 3.6 |
| L4 | 3 | 3.2 |
| L5 | 3 | 2.6 |
| L6 | 3 | 2.5 |
| L7 | 3 | 2.9 |
| L8 | 3 | 2.7 |
| L9 | 3 | 2.0 |
| L10 | 3 | 2.4 |
| L11 | 3 | 2.2 |
| L12 | 3 | 2.1 |
| L13 | 3 | 2.0 |
| L14 | 3 | 0.9 |
| L15 | 3 | 0.9 |

**Table 3**
DOS values, as measured by DL-EPR technique, for various annealing treatment after 5% cold-work, value in bracket show the results of ASTM A 262 Practice A.

| Annealing treatment | Annealed | 575 °C for 1 h | 675 °C for 1 h |
|---|---|---|---|
| 1027 °C for 0.5 h | 0.11 (step) | 0.37 (step) | 1.35 (dual) |
| 1027 °C for 1 h | 0.12 (step) | 0.40 (step) | 0.49 (dual) |
| 927 °C for 24 h | 0.10 (step) | 0.03 (step) | 0.28 (step) |
| 927 °C for 48 h | 0.16 (step) | 0.07 (step) | 0.18 (step) |
| 927 °C for 72 h | 0.20 (step) | 0.10 (step) | 0.12 (step) |

### 3.3. Electrochemical characterization of RIS

Fig. 5a depicts the damage vs. depth profiles for the irradiation levels of 0.86 and 1.00 dpa, as calculated by Eq. (1). As depicted in the Fig. 5a, the damage profile due to 4.8 MeV energy protons consists of the uniform damage region for the first 70 μm of depth followed by the peak damage region up to 80 μm depth from the as-irradiated surface. The fitted curves for damage vs. depth (obtained using Eq. (2)) are plotted in Fig. 5a along with the damage profile obtained using SRIM. The DL-EPR values for the specimens irradiated to 0.86 and 1.00 dpa for different depths are depicted in Fig. 5b. The DL-EPR values for different depths from the surface were fitted using Eq. (2) and plotted simultaneously in Fig. 5b. The values of constants $a$, $b$, $c$ and $x_o$ (the standard deviation shown in bracket)

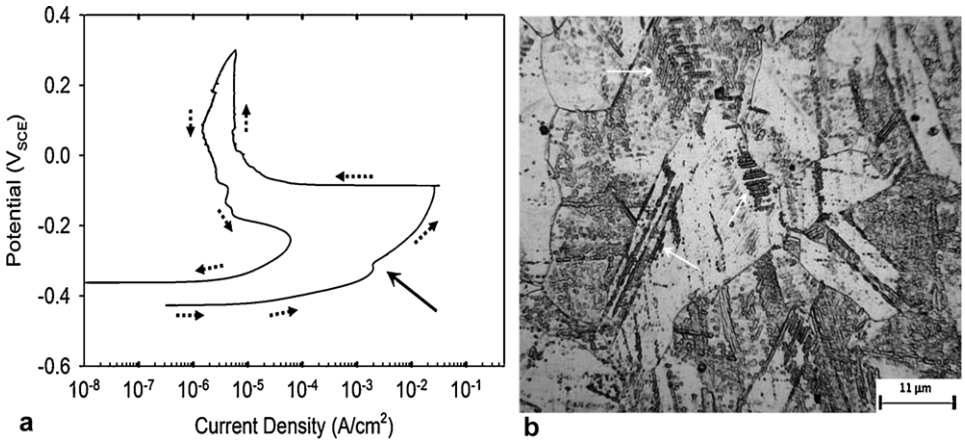


**Fig. 4.** (a) DL-EPR curve for 5% cold-worked specimen, strain-annealed at 1050 °C for 0.5 h (un-irradiated), illustrating an additional peak (marked with an arrow) during the forward scan and (b) optical micrograph of the same specimen after potentiostatic holding at −30 $mV_{SCE}$ for 30 min, showing presence of strained/twinned regions within grains.

for the specimen irradiated to 0.86 dpa are 1.08 (0.07), 1.96 (0.18), 1.00 (0.27) and 76.39 (0.12), respectively. For the specimen irradiated to 1.00 dpa, the corresponding values were 1.37 (0.55), 6.39 (4.64), 1.00 (2.86) and 47.89 (5.82), respectively.

As seen from Fig. 5b, the nature of the fitted-curve of the DL-EPR value vs. depth follows a trend similar to that of the damage vs. depth profile, as calculated by Eq. (1). The SRIM calculation predicts maximum damage at 74 μm whereas, the maximum damage for the specimen irradiated to 0.86 dpa and 1.00 was found at the depth of 90 and 50 μm, respectively. Also, as shown in Fig. 5b, DL-EPR values for the specimen irradiated to 0.86 dpa in the uniform damage region did not follow the trend predicted by Eqs. (1) and (2). The average and maximum DL-EPR values for the specimens irradiated to 0.86 and 1.00 dpa are depicted in Fig. 5c. The extent of damage in the specimen irradiated to 1.00 dpa (higher dose rate) in the uniform damage region was lower as compared to that in

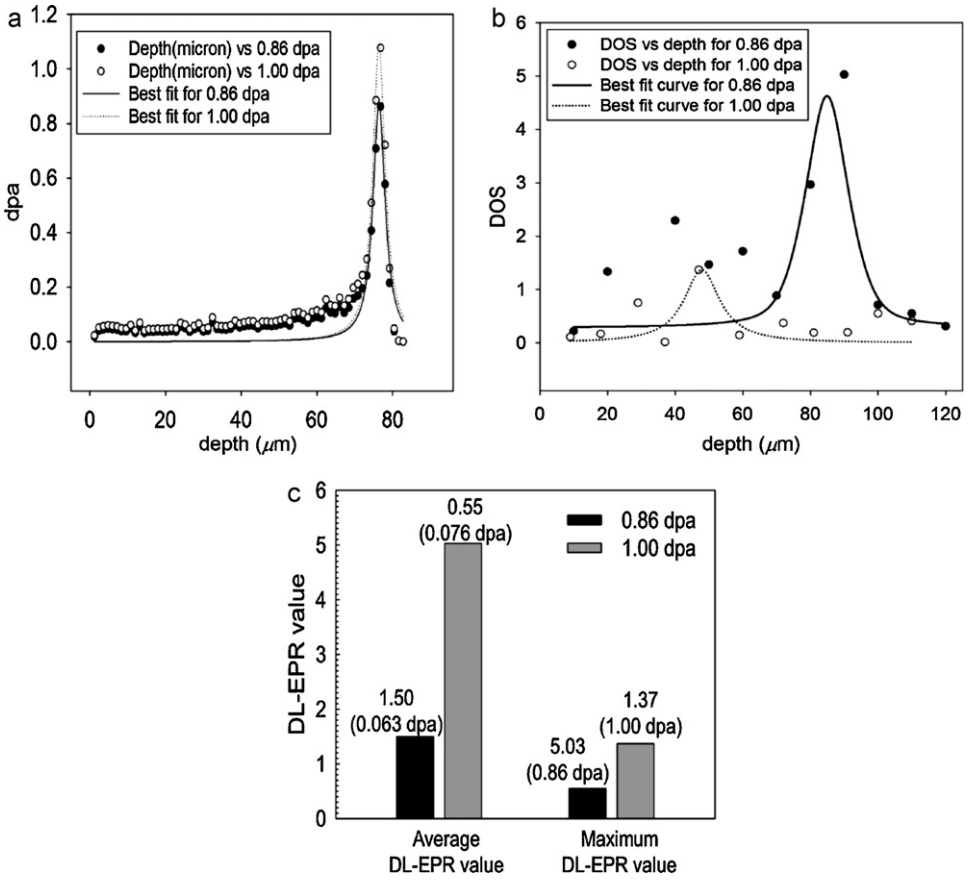


**Fig. 5.** Graphical representations of proton-irradiation damage and DL-EPR results for the ARTW for irradiation levels of 0.86 dpa and 1.00 dpa, (a) SRIM profiles for dpa vs. depth fitted with Eq. (2), showing the uniform damage and the peak damage regions, (b) DL-EPR values vs. depth profiles along with best fit curves (using Eq. (2)) showing maximum attack at depths of 90 and 50 μm for the ARTW specimens irradiated to 0.86 and 1.00 dpa, respectively, and (c) average and maximum DL-EPR values for irradiated specimens, the average and the maximum DL-EPR values for the ARTW specimen irradiated to 0.86 dpa (lower dose rate) were higher than corresponding values for the same specimen irradiated to 1.00 dpa with higher dose rate.

**Table 4**
Flade potentials for the specimen irradiated to 0.86 dpa.

| Depth (μm) | Potential ($mV_{SCE}$) |
|---|---|
| 0 | −120 |
| 10 | −20 |
| 20 | −27 |
| 40 | −31 |
| 50 | −75 |
| 60 | 0 |
| 70 | +65 |
| 80 | +91 |
| 90 | +133 |
| 100 | +99 |
| 110 | +25 |
| 120 | +25 |
| 130 | −69 |

the specimen irradiated to 0.86 dpa (lower dose rate). The maximum damage, indicated by the maximum DL-EPR value, was also lower for the specimen irradiated to 1.00 dpa (higher dose rate) as compared to the specimen irradiated to 0.86 dpa (lower dose rate).

The Flade potentials for the specimen irradiated to 0.86 dpa for different depths from the surface is given in the Table 4. The Flade potential is a potential at which the passivity breaks during the reverse loop of the DL-EPR test and the current begins to increase continuously until it reaches the maximum value. The typical Flade potential value for type 304 SS in the EPR solution is $-200\,mV_{SCE}$ as shown in Fig. 5a. As can be seen from the Table 4, the Flade potential increases with the depth reaching maximum value in the peak damage region. Thus, the Flade potentials at various depths for the specimen irradiated to 0.86 dpa were more positive (anodic) as compared to the typical value for type 304 SS. Also, the values of the Flade potential in the peak damage region were higher than that in the uniform damage region. For the specimen irradiated to 1.00 dpa (higher dose rate), the Flade potentials were in the range of −95 to $-215\,mV_{SCE}$ with the average Flade potential of approximately $-180\,mV_{SCE}$. Thus, for the specimen irradiated to 1.00 dpa, the Flade potentials were comparatively lower. Most of the DL-EPR tests on the ARTW material irradiated to 1.00 dpa (higher dose rate) did not show the reactivation peak during the reverse loop. The DL-EPR value in such cases was calculated using the current density in the potential range of $-0.25$ to $-0.30\,V_{SCE}$.

### 3.4. Optical microscopic examination after DL-EPR

Fig. 6a and b depicts the optical micrographs after the DL-EPR test on the as-irradiated surface for the specimens irradiated to 0.86 and 1.00 dpa, respectively. The microstructure for the specimen irradiated to 0.86 dpa was the typical structure of austenitic grains whereas for the specimen irradiated to 1.00 dpa and it was not the typical austenitic grain structure. The DL-EPR test for the as-irradiated surface of the specimen irradiated to 1.00 dpa did not show the typical active-passive behaviour of type 304 SS in the EPR solution. The current remained approximately constant at 2.00 $\mu A/cm^2$ during the forward as well as the backward loop. The dose rate used for the specimen irradiated to 1.00 dpa was higher than that used for the specimen irradiated to 0.86 dpa. The beam current for the specimen irradiated to 1.00 dpa was in the range of 800–1000 nA. It is possible that a higher dose rate and a higher beam current had altered the microstructure of the as-irradiated surface of the specimen irradiated to 1.00 dpa. Fig. 6c depicts the

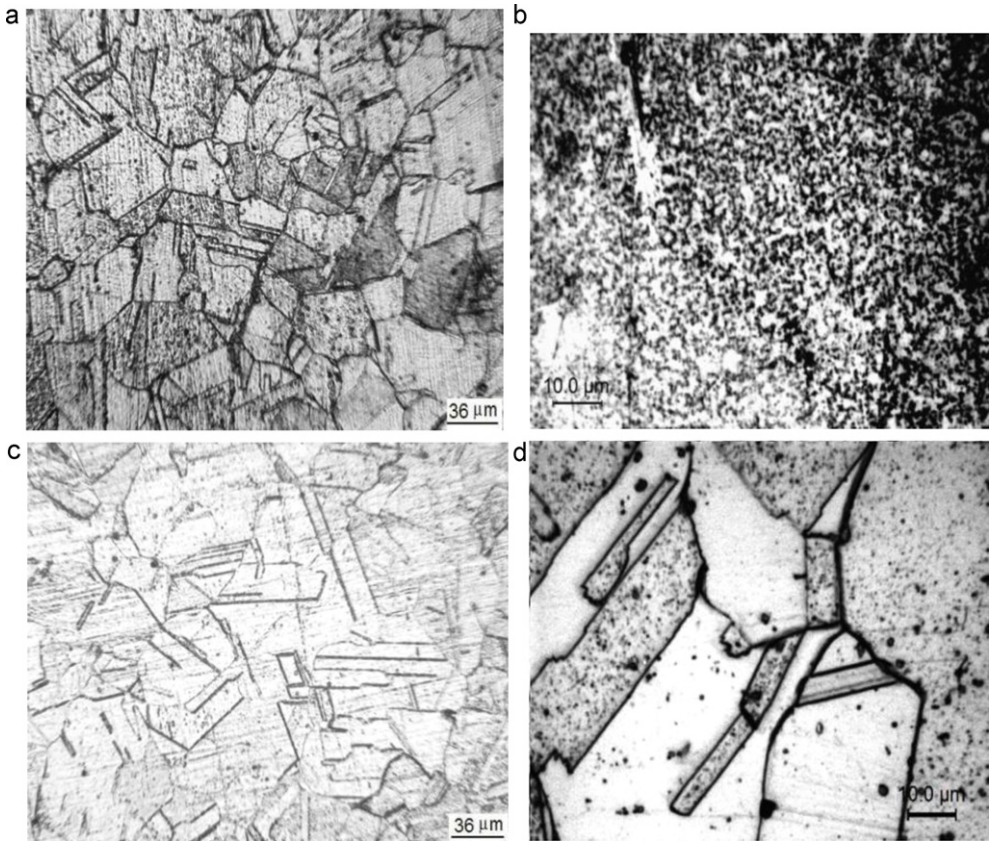


**Fig. 6.** Optical micrographs of proton-irradiated ARTW specimens after the DL-EPR tests (a) at the as-irradiated surface for the specimen irradiated to 0.86 dpa, (b) at the as-irradiated surface for the specimen irradiated to 1.00 dpa, as-irradiated surface of this specimen did not show typical active–passive behaviour during the DL-EPR test, (c) at the depth of 90 μm (0.86 dpa, maximum DL-EPR value: 5.03), most of twin boundaries got attacked, no pit-like features were noticed, and (d) 50 μm depth (1.00 dpa, maximum DL-EPR value 1.37) showing attack on twin boundaries, a few grain boundaries and on pit-like features within grains.

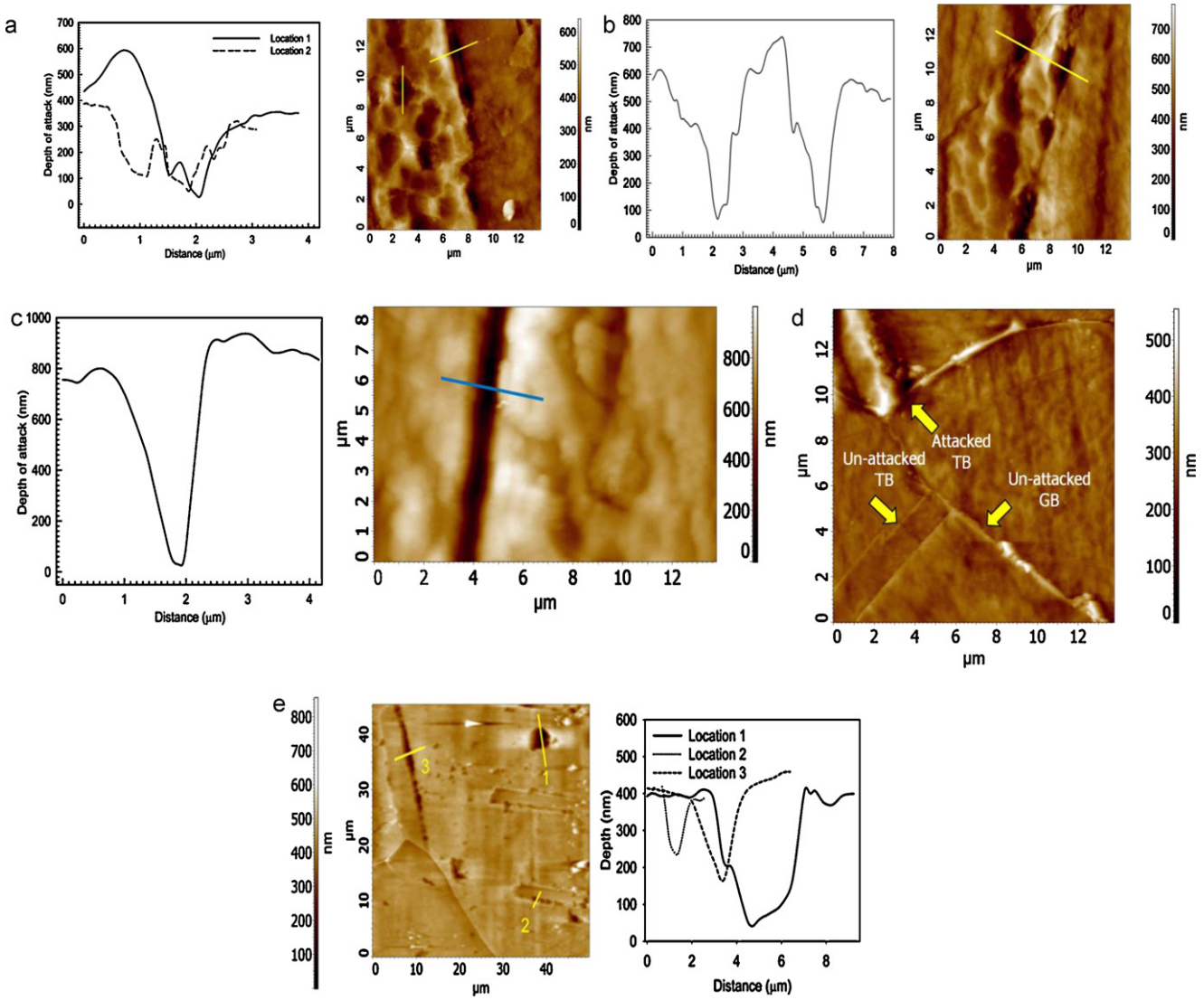


**Fig. 7.** AFM images for irradiated ARTW specimens after the DL-EPR tests (a) at the depth of 90 μm (0.86 dpa), showing discrete attack on a twin-boundary (location 1) with the depth of attack 600 nm. The grain matrix at this location was also got attacked and the depth of attack at the location 2 was 400 nm, (b) at depth of 90 μm (0.86 dpa), depicting attack on grain boundaries, the depth of attack was in the range of 600–700 nm, (c) at the depth of 90 μm (0.86 dpa), showing continuous on a twin-boundary with the depth of attack 900 nm, (d) at the depth of 90 μm (0.86 dpa), showing an affected twin-boundary and an un-affected twin boundary and grain boundary, and (e) at the depth of 50 μm (1.00 dpa), illustrating attack on three different microstructural features, location 1 (pit-like feature within grains), location 2 (discrete attack on a twin-boundary) and location 3 (continuous attack on another twin boundary).

micrograph after the DL-EPR test for the specimen irradiated to 0.86 dpa at the depth of 90 μm with the maximum DL-EPR value of 5.03. The attack was noticed on many twin boundaries and on a few grain boundaries. It was observed that both coherent and incoherent portion of the twin boundaries got attacked during the DL-EPR test. The pit-like features within grains were negligible in this specimen. The number of twin boundaries attacked at 90 μm (maximum DL-EPR attack) was higher as compared to that at other depths at which lower DL-EPR values were obtained. Image analysis of optical micrographs at the depth of maximum DL-EPR value revealed that 80% of twin boundaries were affected and 25% of grain boundaries were affected at the depth of 90 μm for this specimen.

For the specimen irradiated to 1.00 dpa, the maximum DL-EPR value of 1.37 was measured at the depth of 50 μm and the microstructure obtained is depicted in Fig. 6d. As observed for the specimen irradiated to 0.86 dpa, twin boundaries and a few grain boundaries got attacked during the DL-EPR test. However, the extent of attack was very less as compared to that for the specimen irradiated to 0.86 dpa. For the specimen irradiated to 1.00 dpa, a few pit-like features were noticed within grains after the DL-EPR test as shown in Fig. 6d. Such pit-like features were earlier reported [45,46,49] after the EPR test of irradiated austenitic stainless steel.

### 3.5. AFM examination after DL-EPR

Fig. 7 collates AFM micrographs for the specimens irradiated to 0.86 and 1.00 dpa at depths of maximum DL-EPR values, illustrating the nature of attack on different microstructural features. Fig. 7a depicts the attack on a twin boundary and degradation within grains in the specimen irradiated to 0.86 dpa at the depth of 90 μm with maximum DL-EPR value of 5.03. The depth of attack on a twin boundary was 600 nm (at location 1) and depth of attack within the grain at location 2 was 300 nm. Uniform degradation of a few grains was noticed as depicted in Fig. 7a. Several twin boundaries had shown discontinuous attack (as illustrated in Fig. 7a) after the DL-EPR test for the specimen irradiated to 0.86 dpa. Fig. 7b shows an AFM image at the same depth illustrating attack on grain boundaries. The depth of attack on grain boundaries at these locations was in the range of 500–700 nm. The maximum depth of attack on twin boundaries at 90 μm depth was approximately

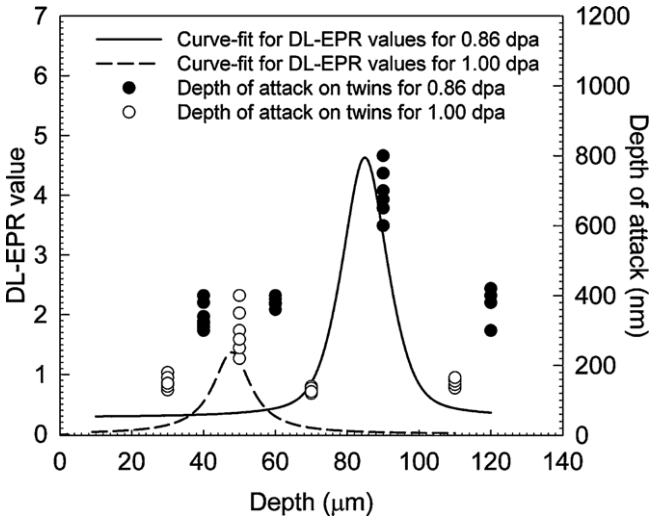


**Fig. 8.** Variation on the depth of attack on twin boundaries after the DL-EPR tests for the ARTW specimens irradiated to 0.86 dpa (lower dose rate) and 1.00 dpa (higher dose rate).The depth of attack on twin boundaries was higher in the specimen irradiated to 0.86 dpa at a comparatively lower dose rate.

800 nm as depicted in Fig. 7c and the overall depth of attack was in the range of 250–800 nm. Fig. 7d depicts an AFM micrograph at the same depth (90 μm, 0.86 dpa) showing three different features viz. a twin-boundary with localized attack, a twin-boundary without any attack and an un-attacked grain boundary, indicating that a few twins remained un-attacked during the DL-EPR test. Fig. 7e shows the AFM micrograph of the specimen irradiated to 1.00 dpa at 50 μm depth (maximum DL-EPR value 1.37) illustrating the attack on three different locations. Location 1 shows the attack on a pit-like feature within grains with the depth of attack of 380 nm, location 2 depicts discrete attack on a twin-boundary with the depth of attack of 180 nm and location 3 shows continuous attack on a twin with the depth of attack of 220 nm. It may be noted that pit-like features observed in the specimen irradiated to 1.00 dpa was not observed for the specimen irradiated to 0.86 dpa.

Fig. 8 summarizes the variation in the depth of attack on twin boundaries for both the irradiated specimens. The curve-fit for DL-EPR values with depth are also plotted in this figure along with the depth of attack on twin boundaries at different depths. As seen from the figure, the depth of attack on twin boundaries in the specimen irradiated to 0.86 dpa was higher than that in the specimen irradiated to 1.00 dpa (higher dose rate). The depth of attack was more at the depth with the maximum DL-EPR value. It is also evident that the depth of attack on twin boundaries was correlated to DL-EPR values at different depths. It may be noted that though less number of grain boundaries got attacked as compared to twin boundaries, the depth of attack on grain boundaries was not less than that at twin boundaries. This is due to the fact that the sink strength of random grain boundaries is very high as compared to twin boundaries.

## 4. Discussion

The hardness of the as-received material (205 HV) was higher than the typical hardness for type 304 SS (180 HV). This indicates the presence of residual strain in the AR material. This was confirmed by line profile (Fig. 2b and d) within a random grain and GAM values (Fig. 2f) for the AR and ARTW material. Strain-annealing treatments at 927 °C for longer time durations after 5% pre-strain had reduced the level of strain within the matrix.

A small pre-strain in low stacking fault energy (SFE) material e.g. type 304 SS facilitates grain boundary migration without new grain formation [56]. A migrating grain boundary inevitably interacts with lattice dislocations and other grain boundaries during grain growth. A low energy grain boundary cannot move a long distance because the absorption rate of lattice dislocations is much lower for a low energy grain boundary than a random boundary [57]. And, migration of low energy grain boundary never occurs before completion of absorption of lattice dislocations. A low energy grain boundary structure is stable and resistant to interactions with defects; therefore, low energy grain boundary tends not to move [58]. Once, low energy grain boundary is produced, it tends to survive for a long time. This suppresses the grain growth once the fraction of special boundaries is increased significantly. In contrast, a high energy grain boundary (random boundary) can migrate over long distance and this increases the interaction with the other boundaries or twin emission to produce low energy grain boundary segments. For a small pre-strain, cross-slip is difficult in low SFE type 304 SS and deformation remains confined to slip planes {1 1 1} in form of linear array of dislocations. This facilitates twin formations in low SFE austenitic material like type 304 SS. Higher values of pre-strain leads to cross-slip and formation of dislocation network structure. Subsequent annealing would lead to formation of new grains instead of twins as in the case of smaller pre-strain values. This ultimately results in formation of higher fraction of special, low-CSL boundaries including twin boundaries. Special boundaries ($\Sigma \leq 29$) are inherently resistant to precipitation reactions due to very low free energy. Thus, the presence of a high fraction of special boundaries in thermo-mechanically treated specimens had improved resistance towards sensitization as indicated by lower DL-EPR values (Table 3) for two heat-treatments at 575 and 675 °C for 1 h. Therefore, on the basis of DL-EPR values, ASTM A 262 Practice A evaluation and high fraction of twin boundaries, the proton irradiation experiments were conducted on the AR material subjected to 5% pre-strain and strain-annealed at 927 °C for 72 h (ARTW).

An additional peak (hump) observed during the forward loop of the DL-EPR test for the specimen with 5% pre-strain followed by strain-annealing at 1027 °C for 0.5 h (shown by an arrow in Fig. 3a) was attributed to strain-regions within the grains that include strain-markings (deformation bands) and twinned regions that were not fully developed. During the forward loop of the DL-EPR test, type 304 SS undergoes general corrosion (dissolution) and different microstructural features dissolve at different rates. The dissolution rates of strain-regions are different than that of the grain matrix leading to appearance of etched strain-regions and an additional peak during the forward loop of the DL-EPR test. Microstructure developed after the potentiostatic hold at $-30\,mV_{SCE}$ in the EPR solution revealed strain-markings and twinned regions (not fully developed) confirming the fact that an addition peak at $-30\,mV_{SCE}$ corresponds to such regions within the grains. It is to be noted that these features (twin regions/strain markings) get attacked in the forward loop even in a specimen that is not subjected to proton irradiation. However, these attacked features are different from the attacked regions that appear due to chromium depletion during the backward (reverse) scan.

The DL-EPR value vs. depth profile (Fig. 5b) for both the irradiated specimens (0.86 and 1.00 dpa) followed a similar trend to that predicted by SRIM calculations, as depicted in Fig. 5a. However, the depths of maximum attack in the DL-EPR tests did not match with SRIM predictions. It may be noted that the SRIM calculation [55] gives the distribution of linear energy transfer due to generation of point defects and energy loss due to phonons. It does not take into account the recombination rate of point defects and presence of different defect sinks within materials. The damage due to proton-irradiation is not only a function of concentrations of point defects but also depends upon crystal structure, recombination rate of point defects and upon various defect sinks present within the

material. Therefore, the presence of defect sinks like grain boundaries, twin boundaries, and dislocations within grains tend to alter the variation of irradiation damage with the depth.

The maximum DL-EPR value for the specimen irradiated to 1.0 dpa was lower than that for the specimen irradiated to 0.86 dpa (Fig. 5b and c). This was due to the fact that the dose rate used for the specimen irradiated to 1.0 dpa was higher than that used for the specimen irradiated to 0.86 dpa. For a higher dose rate at a given temperature, higher is the concentration of point defects within a cascade in a given time frame [59]. The higher concentration of point defects in a fixed time frame leads to a higher probability of recombination of point defects because the thermal mobility does not change. This leads to a lower concentration of freely migrating defects, which are responsible for RIS [29]. Therefore, the higher the dose rate, lesser the number of freely migrating defects and hence lesser the RIS and the attack during the subsequent EPR test.

The results obtained in the present investigation have shown (Fig. 6c and d) that most of the attack had occurred on the twin boundaries and a small fraction of grain boundaries had been attacked during the DL-EPR test after the proton-irradiation. Earlier investigations [36–40] on the effect of grain boundary character on RIS had reported that the level of chromium depletion on $\Sigma 3$ twin boundaries is less as compared to that at random boundaries. However, earlier investigations [36–40] were carried out on austenitic stainless steel without any thermo-mechanical treatments. The fraction of twin boundaries in materials used in previously reported studies [36–40] was not very high as compared to the ARTW material used in the present investigation. Most of the attack during the DL-EPR tests were confined to twin boundaries and a very few random grain boundaries got attacked. The observed attack on twin boundaries during the DL-EPR tests of proton-irradiated specimens can be explained as follows.

The typical interfacial energies of coherent, incoherent and random boundaries at 670 °C are reported to be 16, 265 and 1026 mJ m$^{-2}$ respectively [60]. The temperature coefficient of the interfacial free energy for random boundary was $d\gamma_{gb}/dT = -0.49$ mJ m$^{-2}$/°C and for twin boundary $d\gamma_{tb}/dT = +0.007$ mJ m$^{-2}$/°C [60]. The negative coefficient for a grain boundary indicates that the interfacial energy increases with decreasing temperature and the positive coefficient indicates that the interfacial energy decreases with decrease in temperature. Assuming a linear behaviour for interfacial energy with temperature [61], the interfacial energies at 300 °C for a coherent twin boundary and a random boundary are 19 and 545 mJ/m$^2$, respectively. Therefore, at the proton-irradiation temperature of 300 °C, the difference between interfacial energy of a random boundary and a coherent twin boundary is reduced considerably as compared that at 670 °C. The interfacial free energy of incoherent twin boundary can be calculated by assuming the ratio $\gamma_{tb}/\gamma_{gb}$ (0.25) constant at all temperatures [49], the interfacial energy at 300 °C would be 136 mJ/m$^2$, here, $\gamma_{tb}$ is the interfacial energy of an incoherent twin boundary. Also, the deviation from the ideal condition of 60°⟨1 1 1⟩ (as shown in Fig. 4) for twin boundaries would also increase the interfacial energy of a twin boundary: the higher the deviation more would be the interfacial energy. The defect sink strength is a function of the available free energy at the interface, hence, higher the interfacial energy higher the sink strength. It may be noted that the free energy required for adsorption of point defects is very less as compared to free energy required for precipitation. Hence, it is likely that even a coherent twin boundary can act as a defect sink.

The defect sink strength (in terms of m$^{-2}$) of the grain boundary can be defined as $S^{GB} = A\sin(\theta/2)$, where $A$ is a parameter in units of the inverse square of the length, $\theta$ is the misorientation angle [38,39]. The sink strength of a twin boundary ($\Sigma 3$) is of the order of $10^{16}$ m$^{-2}$ and that of a random boundary is the order of $10^{19}$ m$^{-2}$ [38,39]. The sink strength of dislocation is of the order of $10^{14}$ m$^{-2}$ [62] and it was reported [63] that dislocations can act as sinks for point defects. Therefore, a twin boundary with higher sink strength than dislocations can also act as a sink for point defects. The fraction of special boundaries ($\Sigma \leq 29$) in the thermo-mechanically processed material was 0.80 and the fraction of $\Sigma 3$ was 0.63 including twin (60°⟨1 1 1⟩) fraction of 0.54. Thus, 54% of all boundaries are twin boundaries and such a high fraction of twin boundaries is evident in Fig. 1. The presence of a high fraction of twin boundaries reduces the effective grain size and increases the probability that freely migrating defects would first encounter a twin boundary rather than a random grain boundary. This in turn reduces the migration of point defects towards grain boundaries and hence reduced the extent of chromium depletion (due to RIS) at grain boundaries. The fraction of random boundaries is only 20% in the ARTW material, thus, the probability that migrating point defects encounter a random boundary is substantially less as compared to the probability that migrating point defects encounter a twin boundary. It is assumed that point defects would migrate to the nearest defect sink, a twin boundary, a random boundary, dislocations or any other defect sinks.

Random grain boundaries are perfect sinks whereas twin boundaries are not perfect sinks for point defects generated due to irradiation. Due to lower interfacial free energy and lower defect sink strength of twin boundaries vis-à-vis random boundaries, the extent of chromium depletion on twin boundaries would be less as compared to those at random boundaries. Both coherent and incoherent regions of twin boundaries got attacked at various depths (of the specimen) indicating that the nature of twins (coherent vs. incoherent) does not have any significant effect on the adsorption of point defects. This in turn indicates that the interfacial energy of a coherent twin is sufficient for point defect adsorption.

Thus a very high fraction of twin boundaries within the material had provided a large area for adsorption of point defects. The adsorption of vacancies at defect sinks leads to depletion of chromium at twin boundaries by inverse Kirkendall mechanism and such chromium depletion regions got attacked during the DL-EPR tests. However, it should be noted that the extent of chromium depletion on twin boundaries could never be equal to that measured on the random boundaries because of its lower interfacial energy and lower defect sink strength.

Due to lower interfacial energy, twin boundaries are inherently resistance to precipitation of $M_{23}C_6$ and a high fraction of twin boundaries leads to improved resistance to sensitization [64,65]. Fig. 9 schematically represents the nature of attack on chromium depletion regions in thermally sensitized and proton-irradiated type 304 SS. Fig. 9a is a schematic representation of the microstructure of the AR (as-received) material with very limited number of twin boundaries and Fig. 9b shows a schematic representation of the ARTW (5% pre-strain followed by strain-annealing at 927 °C for 72 h) material with a high fraction of twin boundaries. Fig. 9c schematically represents the nature of attack after the DL-EPR test in the sensitized austenitic stainless steel with high fraction of twin boundaries. In such a material, the presence of twin boundaries breaks continuity of chromium depletion regions. In contrast to grain boundaries, there is very limited connectivity between twin boundaries. Therefore, the connectivity between chromium depletion regions formed on different twin boundaries due to RIS would be very limited (Fig. 9d) and this prevents formation of continuous chromium depletion regions. This is in contrast to formation of chromium depletion regions due to $M_{23}C_6$ at grain boundaries in type 304 SS material with a high fraction of special/twin boundaries [50]. Therefore, the network of chromium depletion regions due to sensitization is interrupted in grain boundary engineered material due the presence of twin boundaries (as shown in Fig. 9c) and in this investigation, chromium depletion regions formed on twin boundaries due to RIS are discrete in nature. Therefore, a high

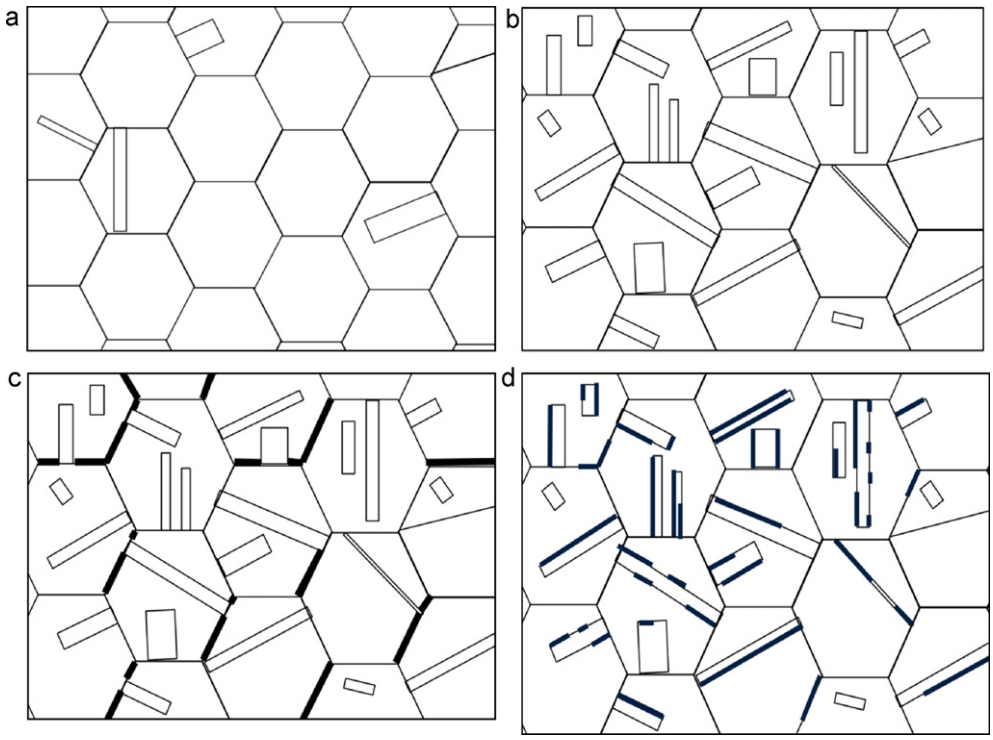


**Fig. 9.** Schematic representation of microstructure in the AR and ARTW material showing (a) the as-received microstructure, with a low fraction of twin boundaries, (b) the microstructure in the ARTW material, with a very high fraction of twin boundaries, (c) the typical microstructure in thermally sensitized ARTW material, showing attack on grain boundaries (thicker boundaries), the presence of twin boundaries disrupting the attack on chromium depletion regions, and (d) the microstructure obtained at the depth of maximum attack in the ARTW specimen irradiated to 0.86 dpa, depicting the attack on twin boundaries with a few grain boundaries also getting attacked.

fraction of twin boundaries led to formation of discontinuous network of chromium depletion regions in both thermally sensitized and proton-irradiated type 304 SS.

The Flade potentials for the ARTW specimen (0.86 dpa, lower dose rate) were more positive implying the passive film over the irradiated surface at different depths was weak. The Flade potential is a measure of the inherent stability of the passive film for stainless steel, higher the Flade potentials weaker the passive films [47]. This could be either due to chromium depletion or due to the higher diffusivities of cation vacancies in the film and/or the metal substrate due to dislocations as suggested by the studies on characterization of passive films on stainless steels [66,67]. Therefore, the presence of point defects generated due to irradiation and chromium depletion had resulted in a weaker passive film, as compared to that on un-irradiated stainless steel, leading to higher Flade potentials. The higher values of the Flade potential in the peak damage region (Table 2) might be due to the fact that the concentrations of point defects and higher chromium depletion were (higher DL-EPR values and higher depth of attack on twin boundaries) higher in the peak damage region as compared to those in the uniform damage region. Higher values of the Flade potentials at depths with lower DL-EPR values indicates that point defects also contribute to an increase in the Flade potential in addition to chromium depletion due to RIS. The Flade potentials for the ARTW specimen irradiated to 1.0 dpa (higher dose rate) were lower as compared to those in 0.86 dpa specimen. It could be due the fact that a higher dose rate used for the specimen irradiated to 1.0 dpa resulted in a lower concentration of freely migrating defects and hence a lower concentration of point defects. Thus, a lower concentration of point defects and limited chromium depleted regions (as indicated by lower maximum DL-EPR value1.37) did not affect the stability of the passive film to the extent as it did in the specimen irradiated to 0.86 dpa.

Higher DL-EPR value (5.03) for the specimen irradiated to 0.86 dpa (lower dose rate) might be due to the fact that the fraction of twin boundaries was very high and 80% of the twin boundaries got attacked at the depth with maximum DL-EPR value. Also, as mentioned in the previous paragraph, the higher Flade potential values indicate a weaker passive film and this led to higher dissolution rate (due to uniform corrosion) as compared to un-irradiated type 304 SS. Thus, a higher DL-EPR value of the ARTW irradiated specimen (0.86 dpa, lower dose rate) might have been due to chromium depletion at twin boundaries and a higher uniform dissolution rate due to a weaker passive film. In addition to that, degradation of the matrix (Fig. 7a) was also noticed for few grains, which contributes to the current during the reactivation loop of the DL-EPR test.

The maximum current density ($i_{max}$) during the reverse loop of the DL-EPR test in the irradiated specimens can be taken as the sum of the current density due to chromium depletion ($i_{depl}$), current density due to dissolution of matrix ($i_{matrix}$), and the current density due to a higher dissolution rate ($i_{pass}$) due to a weaker passive film. In a typical thermally sensitized type 304 SS, the contribution of $i_{pass}$ to the maximum current density during EPR would be negligible because the passive film would be the weak only over the localized chromium depletion regions and in case of irradiated type 304, the passive film would be more weaker due to the presence of point defects.

It may be noted that attack on twin boundaries after the DL-EPR test in proton-irradiated desensitized type 304 SS was also observed in an earlier investigation [68]. However, the depth of attack was more on random grain boundaries than that on twin boundaries [68]. This is in agreement with results obtained in the present investigation that twin boundaries can also act as defect sinks leading to chromium depletion due to RIS. Some of twin boundaries remained un-attacked (at the depth of maximum attack, 90 μm for the ARTW specimen irradiated to 0.86 dpa) during the DL-EPR test (Fig. 7d). The possible reason could be a very minor deviation from the ideal twin condition ($60^\circ\langle 1\,1\,1\rangle$) which

reduces the interfacial energy of coherent twin boundaries. Thus, twin boundaries with very minor deviation from the ideal twin condition might have a comparatively lower defect sink strength and hence, a negligible attack on such boundaries.

## 5. Conclusions

Effects of a high fraction of twin boundaries and of dose rate on radiation-induced segregation in austenitic type 304 stainless steel were investigated using proton-irradiation at 300 °C. Double loop-electrochemical potentiokinetic reactivation followed by atomic force microscopic examination was used to characterize RIS in type 304 SS. Following conclusions are derived:

(1) The presence of a high fraction twin boundary had restricted migration of point defects towards grain boundaries and the preferential adsorption of point defects had occurred at twin boundaries. This led to chromium depletion at twin boundaries as indicated by higher DL-EPR values and attacked twin boundaries after the EPR test.
(2) The adsorption of point defects therefore occurs at the nearest defect sinks first encountered during migration—be it a twin boundary or a random grain boundary.
(3) The attack on coherent twin boundaries was noticed after the DL-EPR test indicating that the interfacial energy of coherent twin boundaries was sufficient for point defect adsorption.
(4) The depth of attack, as measured by AFM examination, was correlated to DL-EPR values and was used to characterize the extent of attack on different microstructural features.
(5) Point defects generated due to irradiation led to higher Flade potential values indicating a weaker passive film on the irradiated stainless steel.
(6) The higher dose rate led to lesser RIS due to the fact that the less number of freely migrating defects were produced because of increased probability of recombination.

## References


[1] T. Watanabe, Res. Mech. 11 (1984) 47–84.
[2] V. Randle, Acta Mater. 52 (2004) 4067–4081.
[3] V. Randle, Acta Mater. 47 (1999) 4187–4196.
[4] I. Karius, W. Gust, Fundamentals of Grain and Interphase Boundary Diffusion, Ziegler Press, Stuttgart, Germany, 1988, p. 275.
[5] H. Kokawa, T. Watanabe, S. Karashima, Philos. Mag. A 44 (1981) 1239.
[6] J.Le. Coze, M. Biscondi, J. Levy, C. Goux, Membr. Sci. Rev. Metall. 70 (1973) 397.
[7] J.Le. Coze, M. Biscondi, Can. Metall. Q 13 (1974) 59.
[8] H.H. Kokawa, M. Shimada, Y.S.Y.S. Sato, JOM 52 (2000) 34.
[9] M. Froment, J. Phys. 36 (1975) c4–c371.
[10] X.R. Qian, Y.T. Chou, Philos. Mag. A 45 (1982) 1075.
[11] H. Kokawa, C.H. Lee, T.H. North, Metall. Trans. A 22 (1991) 1627.
[12] P.H. Pumphrey, in: G.A. Chadwick, D.A. Smith (Eds.), Special High Angle Boundaries, Grain Boundary Structure and Properties, Academic Press, London, 1976, p. 139.
[13] M.S. Laws, P.J. Goodhew, Acta Metall. Mater. 39 (1991) 1525–1533.
[14] H.U. Hong, B.S. Rho, S.W. Nam, Mater. Sci. Eng. A 318 (2001) 285–292.
[15] H.U. Hong, S.W. Nam, Mater. Sci. Eng. A 332 (2002) 244–261.
[16] E.A. Trillo, L.E. Murr, Acta Mater. 47 (1998) 235–245.
[17] Richard Jones, Valerie Randle, Mater. Sci. Eng. A 527 (2010) 4275–4280.
[18] M. Michiuchi, H. Kokawa, Z.J. Wang, Y.S. Sato, K. Sakai, Acta Mater. 54 (2006) 5179–5184.
[19] M.H. Kokawa, Z.J. Wang, Y.S. Sato, I. Karibe, Acta Mater. 50 (2002) 2331–2341.
[20] W. Jin, S. Yang, H. Kokawa, Z. Wang, Y.S. Sato, J. Mater. Sci. Technol. 23 (2007) 785–789.
[21] H. Kokawa, M. Shimada, M. Michiuchi, Z.J. Wang, Y.S. Sato, Acta Mater. 55 (2007) 5401–5407.
[22] M. Qian, J.C. Lippold, Acta Mater. 51 (2003) 3351.
[23] V. Randle, H. Davies, Metall. Mater. Trans. A 33 (2002) 1853.
[24] D.N. Wasnik, V. Kain, I. Samajdar, B. Verlinden, P.K. De, Acta Mater. 50 (2002) 4587–4601.
[25] D. Wasnik, V. Kain, I. Samajdar, B. Verlinden, P.K. De, J. Mater. Eng. Perform. 12 (2003) 402–407.
[26] D.N. Wasnik, V. Kain, I. Samajdar, B. Verlinden, P.K. De, Mater. Sci. Forum 467–470 (2004) 813–818.
[27] G. Palumbo, K.T. Aust, in: D. Wolf, S. Yip (Eds.), Materials Interfaces, Chapman and Hall, London, 1992, p. 190.
[28] V. Kain, P.K. De, S. Banerjee, Proc. Intl. Conf. on Corrosion CORCON'92, Elsevier, Mumbai, Dec 3–6, 1997, pp. 258–269.
[29] S.M. Bruemmer, E.P. Simonen, P.M. Scott, P.L. Andresen, G.S. Was, J.L. Nelson, J. Nucl. Mater. 274 (1999) 299.
[30] M.J. Hackett, R. Najafabadi, G.S. Was, J. Nucl. Mater. 389 (2009) 279–287.
[31] M.J. Hackett, J.T. Busby, G.S. Was, Met. Mater. Trans. 39A (2008) 218–224.
[32] G.S. Was, P.L. Andresen, J. Mater. 44 (1992) 8.
[33] G.S. Was, S.M. Bruemmer, J. Nucl. Mater. 216 (1994) 326.
[34] J.T. Busby, M. Hash, G.S. Was, J. Nucl. Mater. 336 (2005) 267–268.
[35] G.S. Was, T.R. Allen, Mater. Charact. 32 (1994) 239–255.
[36] T.S. Duh, J.J. Kai, F.R. Chen, L.H. Wang, J. Nucl. Mater. 258–263 (1998) 2064–2068.
[37] T.S. Duh, J.J. Kai, F.R. Chen, J. Nucl. Mater. 283–281 (2000) 198–204.
[38] S. Watanabe, Y. Takamatsu, N. Sakaguchi, H. Takahashi, J. Nucl. Mater. 283–287 (2000) 152–156.
[39] S. Watanabe, Y. Takamatsu, N. Sakaguchi, H. Takahashi, J. Phys. IV 10 (2000), Pr6-173-Pr6-178.
[40] N. Sakaguchi, S. Watanabe, H. Takahashi, R.G. Faulkner, J. Nucl. Mater. 329–333 (2004) 116–1169.
[41] V. Kain, R.C. Prasad, P.K. De, Corrosion 58 (2002) 15–38.
[42] V. Kain, Y. Watanabe, J. Nucl. Mater. 302 (2002) 49.
[43] K. Kondou, A. Hasegawa, K. Abe, V. Kain, Y. Watanbe, Proceedings of 10th international conference on Degradation of Materials in Nuclear Power Systems—Water Reactors, Paper No.66, Nevada, American Nuclear Society and National Association of Corrosion Engineers, August 1991.
[44] R. Katsura, S. Nishimura, NACE Annual Conference and Corrosion Show, Paper No.91, CORROSION 92, 1992.
[45] G.E.C. Bell, T. Inazumi, E.A. Kenik, T. Kondo, J. Nucl. Mater. 187 (1992) 170–179.
[46] K. Kondou, A. Hasegawa, K. Abe, J. Nucl. Mater. 329–333 (2004) 652–656.
[47] T. Inazumi, G.E.C. Bell, E.A. Kenik, K. Kiuchi, Corrosion 46 (1990) 786.
[48] T. Inazumi, G.E. Bell, A. Hishinuma, Corrosion/90, National Association of Corrosion Engineers, Paper No. 507, 1990.
[49] P. Ahmedabadi, V. Kain, K. Arora, I. Samajdar, Corros. Sci. 53 (2011) 1465–1475.
[50] H.Y. Bi, H. Kokawa, Z.J. Wang, M. Shimada, Y.S. Sato, Scripta Mater. 49 (2003) 219–223.
[51] D.G. Brandon, Acta Metall. 14 (1966) 1479–1484.
[52] M.J. Norgett, M.T. Robinson, I.M. Torrens, Nucl. Eng. Des. 33 (1975) 30.
[53] Annual Book of Standard, ASTM A262-10, Practice A, Standard Practices for Detecting Susceptibility to Intergranular Attack in Austenitic Stainless Steels, vol. 1.03, ASTM International, PA, 2010.
[54] A.P. Majidi, M.A. Steicher, Corrosion 40 (1984) 584–593.
[55] J.F. Ziegler, J.P. Biersack, SRIM2003 Program, IBM Corp, Yorktown, NY, 2003.
[56] M. Shimada, H. Kokawa, Z.J. Wang, Y.S. Sato, I. Karibe, Acta Mater. 50 (2002) 2331–2341.
[57] H. Kokawa, T. Watanabe, S. Karashima, J. Mater. Sci. 18 (1983) 1183.
[58] H. Kokawa, T. Watanabe, S. Karashima, Scripta Metall. 17 (1983) 1155.
[59] G.S. Was, Fundamentals of Radiation Materials Science, First ed., Springer Verlag, 2007, p. 245.
[60] E.A. Trillo, L.E. Murr, J. Mater. Sci. 33 (1998) 1263–1271.
[61] L.E. Murr, G.I. Wong, R.J. Horylev, Acta. Metall. Mater. 21 (1973) 595–604.
[62] G.R. Odette, M.J. Alinger, B.D. Wirth, Annu. Rev. Res. 38 (2003) 471–503.
[63] W. Karlsen, S. Van Syck, J. Nucl. Mater. 406 (2010) 127–137.
[64] Richard Jones, Valerie Randle, Gregory Owen, Mater. Sci. Eng. A 496 (2008) 256–261.
[65] Valerie Randle, Richard Jones, Mater. Sci. Eng. A 524 (2009) 134–142.
[66] C.Y. Chao, L.F. Lin, D.D. Macdonald, J. Electrochem. Soc. 128 (1991) 1187.
[67] M. Urduidi-Macdonald, D.D. Macdonald, J. Electrochem. Soc. 134 (1987) 41.
[68] P. Ahmedabadi, V. Kain, K. Arora, I. Samajdar, S. Sharma, P. Bhagwat, J. Nucl. Mater., doi:10.1016/j.jnucmat.2011.06.024.